ADVANCED FUNCTIONAL MATERIALS
www.afm-journal.de

# Myeloid-Derived Suppressor Cell Membrane-Coated Magnetic Nanoparticles for Cancer Theranostics by Inducing Macrophage Polarization and Synergizing Immunogenic Cell Death

*Guang-Tao Yu, Lang Rao, Hao Wu, Lei-Lei Yang, Lin-Lin Bu, Wei-Wei Deng, Lei Wu, Xiaolin Nan, Wen-Feng Zhang, Xing-Zhong Zhao, Wei Liu,* and Zhi-Jun Sun**

**A major challenge for traditional cancer therapy, including surgical resection, chemoradiotherapy, and immunotherapy, is how to induce tumor cell death and leverage the host immune system at the same time. Here, a myeloid-derived suppressor cell (MDSC) membrane-coated iron oxide magnetic nanoparticle (MNP@MDSC) to overcome this conundrum for cancer therapy is developed. In this study, MNP@MDSC demonstrates its superior performance in immune evasion, active tumor-targeting, magnetic resonance imaging, and photothermal therapy (PTT)-induced tumor killing. Compared with red blood cell membrane-coated nanoparticles (MNPs@RBC) or naked MNPs, MNP@MDSCs are much more effective in active tumor-targeting, a beneficial property afforded by coating MNP with membranes from naturally occurring MDSC, thus converting the MNP into "smart" agents that like to accumulate in tumors as the source MDSCs. Once targeted to the tumor microenvironment, MNPs@MDSC can act as a PTT agents for enhanced antitumor response by inducing immunogenic cell death, reprogramming the tumor infiltrating macrophages, and reducing the tumor's metabolic activity. These benefits, in combination with the excellent biocompatibility and pharmacological kinetics characteristics, make MNP@MDSC a promising, multimodal agent for cancer theranostics.**

## 1. Introduction

Up to now, cancer remains a major public health problem, causing over 14 million deaths around the world annually.[1] The current mainstay of cancer therapy besides surgical resection for physical removal of the tumor mass, are chemoradiotherapy and more recently immunotherapy to induce tumor cell death and leverage the host immune system, respectively.[2] A major challenge with these regimens, however, is how to induce tumor cell death and enhance host antitumor immune response at the same time. Fortunately, the application of nanotechnology makes traditional medicine become intelligent depending on the characteristics of nanoparticles, such as the size on the nanometer scale enables them enhanced permeability and retention effect (EPR) and the high surface-area-to-volume ratio enables them to be wrapped with various modified compounds (e.g., antibody or cell membrane).[3] Among these nanoparticles, iron oxide nanoparticles have been widely used for drug carriers, magnetic resonance imaging (MRI), and photothermal therapy (PTT) in tumor biological applications.[4] More recently, ferumoxytol, a FDA-approved $Fe_3O_4$ nanoparticle, was confirmed to transform M2 macrophages to M1 macrophages for improving antitumor immune response in tumor environment based on Fenton reaction.[5] However, simply increasing the number of M1 macrophages is not significantly enough to promote antitumor immune response due to tumor cells hide itself immunogenicity.

Myeloid-derived suppressor cells (MDSCs), a heterologeneous population of immature myeloid lineage cells, are

G.-T. Yu, H. Wu, L.-L. Yang, Dr. L.-L. Bu, W.-W. Deng, L. Wu, Prof. W.-F. Zhang, Prof. Z.-J. Sun
The State Key Laboratory Breeding Base of Basic Science of Stomatology and Key Laboratory of Oral Biomedicine
Ministry of Education and Department of Oral Maxillofacial-Head Neck Oncology
School and Hospital of Stomatology
Wuhan University
Wuhan, Hubei 430079, China
E-mail: sunzj@whu.edu.cn

The ORCID identification number(s) for the author(s) of this article can be found under https://doi.org/10.1002/adfm.201801389.

DOI: 10.1002/adfm.201801389

L. Rao, Dr. L.-L. Bu, Prof. X.-Z. Zhao, Prof. W. Liu
Key Laboratory of Artificial Micro- and Nano-Structure of Ministry of Education School of Physics and Technology
Wuhan University
Wuhan, Hubei 430072, China
E-mail: wliu@whu.edu.cn

L. Wu, Prof. X. Nan
Department of Biomedical Engineering, Center for Spatial Systems Biomedicine, and Center for Cancer Early Detection Advanced Research Knight Cancer Institute
Oregon Health and Science University
Portland, OR 97201, USA

present in low number in healthy individuals.[6] Due to MDSC as a major regulator of immune responses in cancer, the immune system not only kills the MDSC, but also will cater to the increase of MDSC.[7] Nevertheless, in tumor patients, MDSCs expeditiously accumulate in the tumor environment, which depends on the surface membrane protein receptors, as a result of chronic inflammation caused by cytokines and chemokines produced by tumors.[8] By translocating the cell membrane from a kind of natural cell onto the surface of a kind of nanoparticle (biomimetic engineering), the cell membrane relevant biological characteristics are transferred, including the surface receptors and antibodies which can possibility be used for immune evasion and active targeting tumor cell or tumor microenvironment.[9]

Based on the characteristics of MDSC and our previous biomimetic engineering experiences,[4e,10] herein, we develop a novel nanoparticle according to present emerging method: the magnetic $Fe_3O_4$ nanoparticle (MNP) was coated with MDSC membranes (MNP@MDSC). The resulting novel nanoparticles, hereafter referred to as MNP@MDSC, exhibit much enhanced antitumor activity for three reasons. First, coating the MNPs with MDSC membrane allows efficient immune escape and targeting to the tumor site, by mimicking the naturally occurring MDSC cells that are nonimmunogenic and have a high affinity to the tumor, thus making the MNP@MDSC a "smart bullet." Compared with MNPs coated with membranes from red blood cells (MNP@RBC) that we reported recently to also have good immune escape capability, the MNP@MDSC should have additional benefits in more efficient active targeting to the tumors. Second, accumulation of MNP@MDSC at the tumor site permits high-contrast tumor imaging with MRI for diagnosis. Third, the efficacy of MNPs in modulating M2 to M1 macrophage polarization can be synergized with PTT-enhanced immunologic cell death (ICD) to enhance antitumor immune response (**Scheme 1**).

## 2. Results and Discussion

### 2.1. Synthesis of MNP@MDSC

Preparation of MNP@MDSC includes three main steps: (i) synthesizing pristine $Fe_3O_4$ nanoparticles, (ii) preparing MDSC membranes, and (iii) fusing MDSC membranes on to the $Fe_3O_4$ nanoparticles. The $Fe_3O_4$ nanoparticles with a diameter of ≈80 nm were synthesized using a modified solvothermal method as described in our previous publication.[4e] MDSCs were acquired from tumor-bearing mice using a Miltenyi sorting kit. The purity of MDSCs was quantified to be higher than 95% with flow cytometry (**Figure 1**a). Membranes of MDSCs were achieved by emptying harvested MDSC of their intracellular contents via a combination of hypotonic lysis, mechanical membrane disruption, and differential centrifugation.[10a] The image of transmission electron microscopy (TEM) demonstrated a $Fe_3O_4$ nanoparticle core of ≈80 nm and an outer lipid bilayer shell of ≈5 nm in thickness (Figure 1b,c). The thickness was in accord with the reported cell membrane of 5–10 nm.[11] After preparation, the fusion of MNP@MDSC remained stable for at least one week in phosphate buffered saline (PBS) or fetal bovine serum (FBS) (Figure S1, Supporting Information). Dynamic light scattering (DLL) analysis showed that the size (hydrodynamic diameter) of MNPs increased from ≈85 to ≈100 nm and the zeta potential from −18 to −13 mV, respectively,

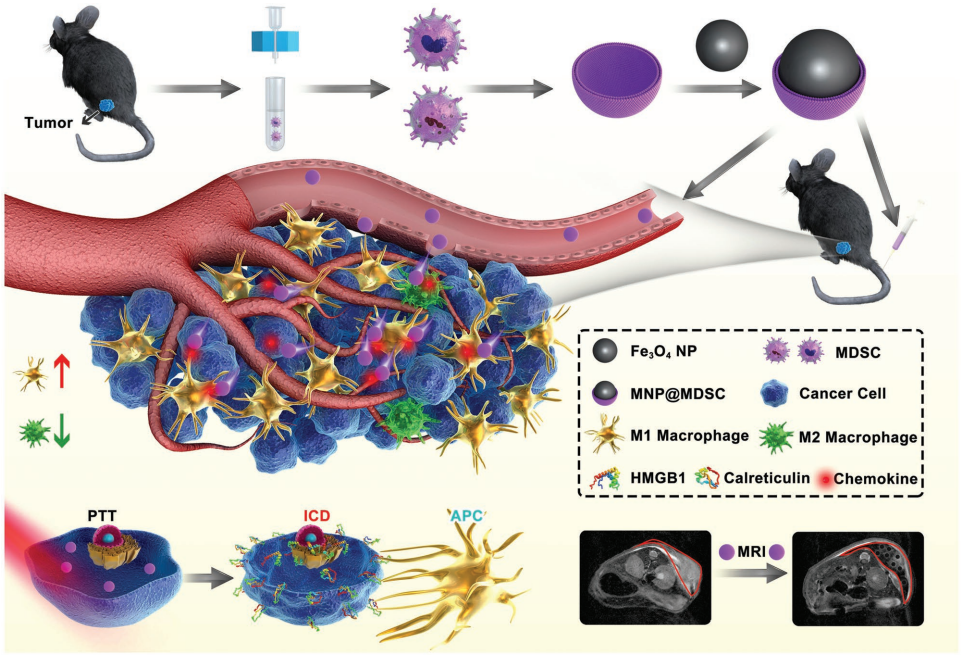


**Scheme 1.** Schematic illustration of the synthesis of MNP@MDSC and its application in cancer theranostics, highlighting: active targeting to the tumor microenvironment; conversion of intratumoral M2 macrophages into M1 macrophages; photothermal therapy inducing immunogenic cancer cell death (ICD) characterized by the elevated expression of HMGB1 and Calreticulin; and utilities for MR imaging.

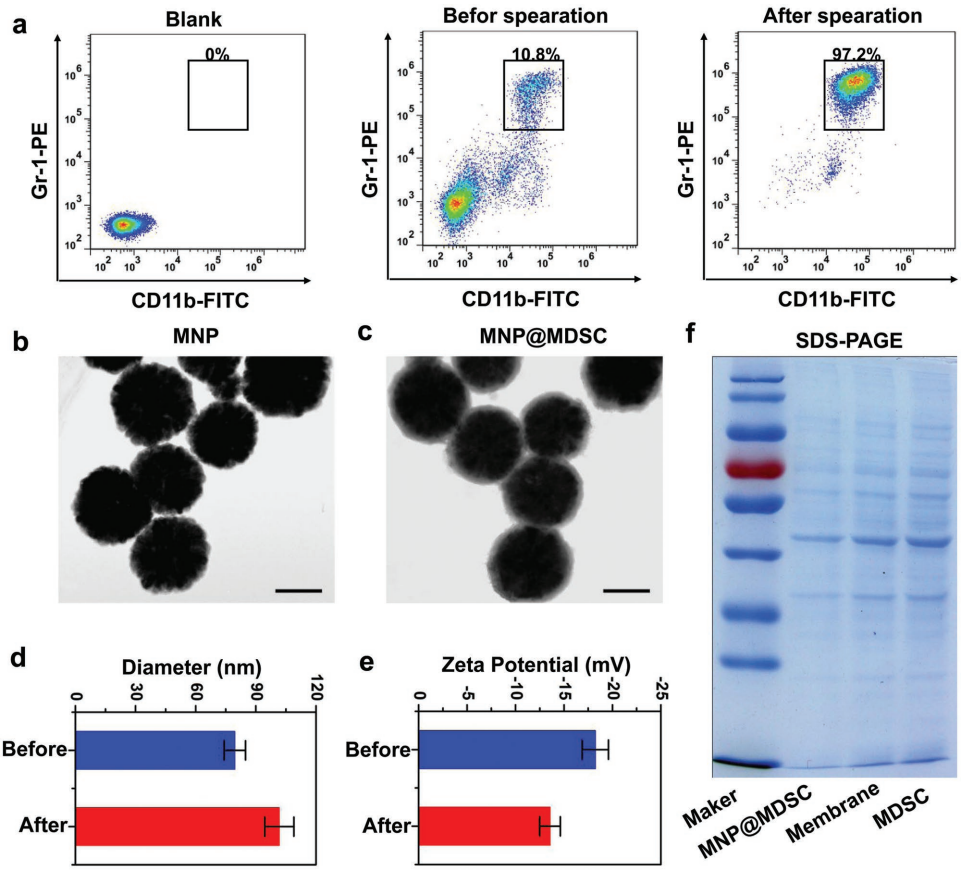


**Figure 1.** Preparation and characterization of MNP@MDSC. a) MDSCs were sorted from tumor-bearing C57BL/6 mice using a Miltenyi sorting kit. b) TEM image of naked MNP. Scale bar = 50 nm. c) TEM image of MNP@MDSC. Scale bar = 50 nm. d) Hydrodynamic size of MNP and MNP@MDSC. e) Zeta potential of MNP and MNP@MDSC. f) Representative SDS-PAGE protein analysis of MDSC, MDSC membranes, and MNP@MDSC.

after coating with MDSC membranes (Figure 1d,e). As a traditional photothermal agent for MNP, temperature curves of these nanoparticles were monitored by an IR camera (Figure S2, Supporting Information), indicating that MNP@MDSC could have been applied as a photothermal agent. Sodium dodecyl sulfate-polyacrylamide gel electrophoresis (SDS-PAGE) stripes further revealed that MDSC membrane transfer did not influence the membrane protein expression in the MNP@MDSC (Figure 1f).

### 2.2. Biosafety of MNP@MDSC In Vivo

We next sought to evaluate the biosafety of MNP@MDSC in vivo, which is a critical factor for future clinical use.[12] In these tests, we included MNP@RBC as a comparison group, as MNP@RBCs were shown to have excellent biosafety. PBS, MNP, MNP@RBC, and MNP@MDSC were injected into ICR mice via tail vein. The changes in body weight were not significantly different among the three nanoparticle groups compared with PBS group (**Figure 2**a), indicating that overall these nanoparticles have little or no side effects on mice. Four weeks after injection, the mice were euthanized for blood biochemistry, hematology, and histological analyses. Key functional indicators of liver and kidney including alkaline phosphatase (ALP), alanine aminotransferase (ALT), aspartate aminotransferase (AST), creatinine (CRE), and blood urea nitrogen (BUN) also showed no significant difference among all the four groups, indicating that intravenous injection of these nanoparticles did not impact the normal function of the liver or kidney (Figure 2b–d). Additionally, we did not observe statistically significant differences in parameters of blood routine in each group (Table S1, Supporting Information). Hematoxylin and eosin (H&E) staining of the harvested heart, liver, spleen, lung, and kidney sections also did not show any signs of abnormality in cellar morphology, inflammation, or tissue organization in the treated group as compared with the normal control group (Figure 2e). Together, these results demonstrate that MNP@MDSC has excellent biocompatible in vivo.

### 2.3. Characterization of Immune Escape and Active Targeting Tumor Microenvironment Effect of MNP@MDSC

The immune system maintains the homeostasis by eliminating the foreign body including bacteria, virus, and abnormal body cells.[13] Strictly speaking, MNP@MDSC is a foreign object to the host and may be eliminated by the immune system like bacteria, virus, and other pathogens.[14]

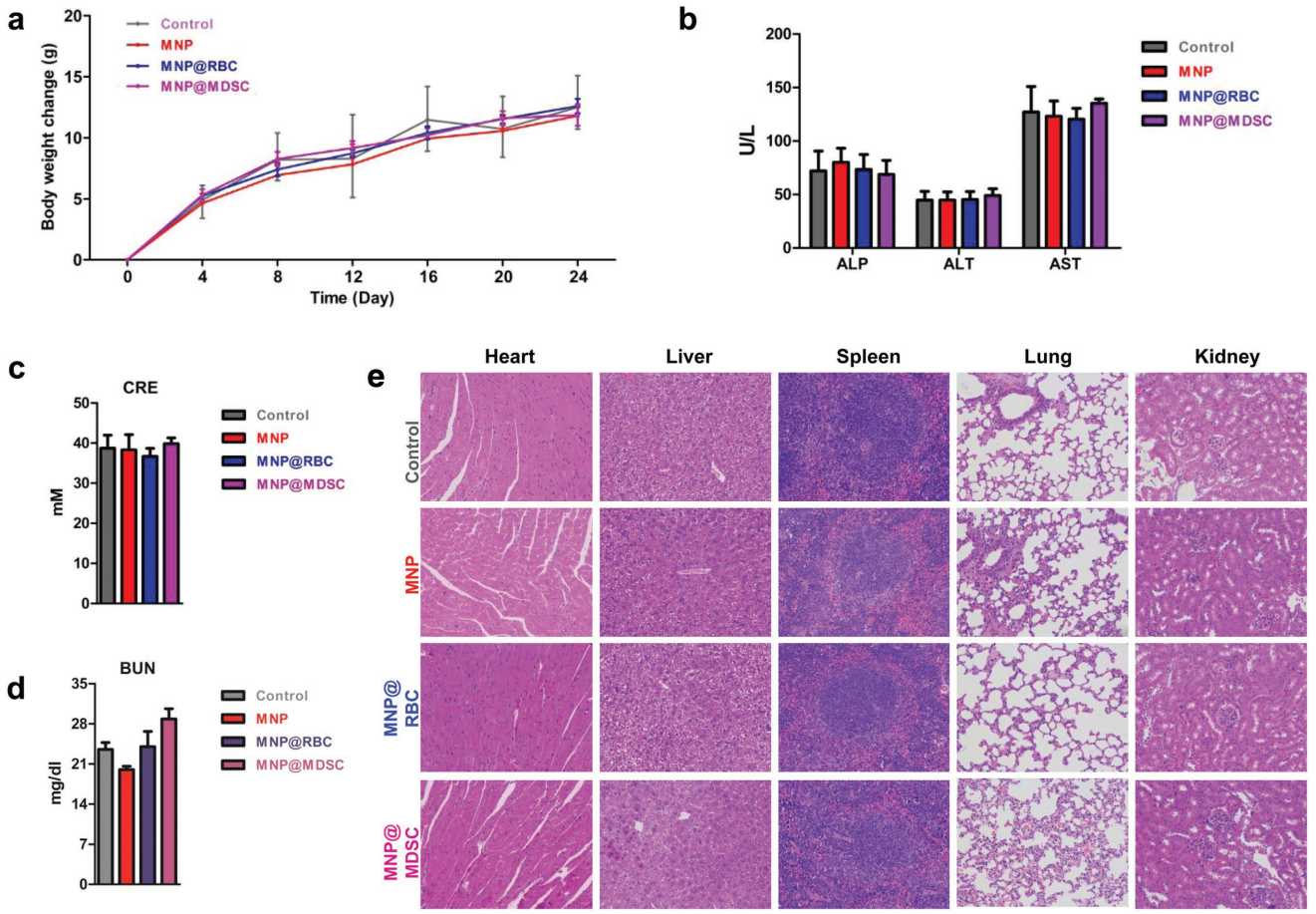


**Figure 2.** In vivo toxicity evaluation. a) Mice body weight curves after intravenous injection of PBS, MNP, MNP@RBC, or MNP@MDSC ($n$ = 5 in each group). b–d) Hepatic and renal function indicators of the mice after intravenous injection of PBS, MNP, MNP@RBC, or MNP@MDSC. (ALP, alkaline phosphatase; ALT, alanine aminotransferase; AST, aspartate aminotransferase; CRE, creatinine; BUN, blood urea nitrogen.) e) Representative histological sections of vital organs (heart, liver, spleen, lung, and kidneys) stained with hematoxylin and eosin at four weeks after intravenous injection of PBS, MNP, MNP@RBC, or MNP@MDSC.

To test the immune escape capability of the MNP@MDSC, we incubated MNP, MNP@RBC, and MNP@MDSC with RAW264.7 murine macrophage cells to testify the uptake of NPs. We found that the cellular uptake of MNP@MDSC was 5–10-fold lower than naked MNP and ≈50% of MNP@RBC at all the doses tested (Figure S3, Supporting Information). Based on this result in vitro, we hypothesized that MNP@MDSC could possess superior immune escape and, as facilitated by the MDSC membrane coating, efficient tumor-targeting capabilities in vivo.

To test this hypothesis, we injected C57BL/6 melanoma mice with MNP, MNP@RBC, and MNP@MDSC via tail vein and assayed tissue uptake of the nanoparticles in terms of Fe content with inductively coupled plasma-atomic emission spectroscopy (ICP-AES). 1 d after injection, the MNP@MDSC group had the highest Fe content in the tumor compared with MNP or even MNP@RBC group (Figure S4a, Supporting Information). Consistently, MNP contents in the tumor tissue were much higher with MNP@MDSC than with naked MNP or MNP@RBC as revealed by Prussian blue staining (Figure S4b, Supporting Information). These results confirmed that the MNP@MDSCs are even more efficient in escaping the host immune clearance and active targeting to the tumor microenvironment.

### 2.4. In Vivo MRI and PTT Effect of MNP@MDSC

Further, to investigate the in vivo pharmacokinetics and biodistribution, we injected MNP, MNP@RBC, or MNP@MDSC (5 mg $mL^{-1}$ in 200 µL PBS) intravenously to ICR mice ($n$ = 4) and measured the Fe concentration in blood at various time points using ICP-AES. Notably, both the MNP@RBC and MNP@MDSC groups exhibited significantly longer circulation time than MNP group (**Figure 3**a). Furthermore, in investigating the in vivo Fe accumulation in major organs at 48 h postinjection, we found that the nanoparticles predominantly accumulated in the liver and the spleen which are the two primary phagocyte-enriched reticuloendothelial systems (RES). Among the four, the MNP@RBC and the MNP@MDSC groups showed significantly lower accumulation in the liver and the spleen than the MNP group (Figure 3b), demonstrating the benefit of MDSC or RBC membrane coating in decreasing RES uptake and maintaining the plasma concentration of MNPs.

The efficient and active targeting of MNP@MDSC to tumors potentially makes these nanoparticles better agents than existing MNPs for MRI and therapy with PTT, two theranostics capabilities afforded by the use of MNPs. We first evaluated the

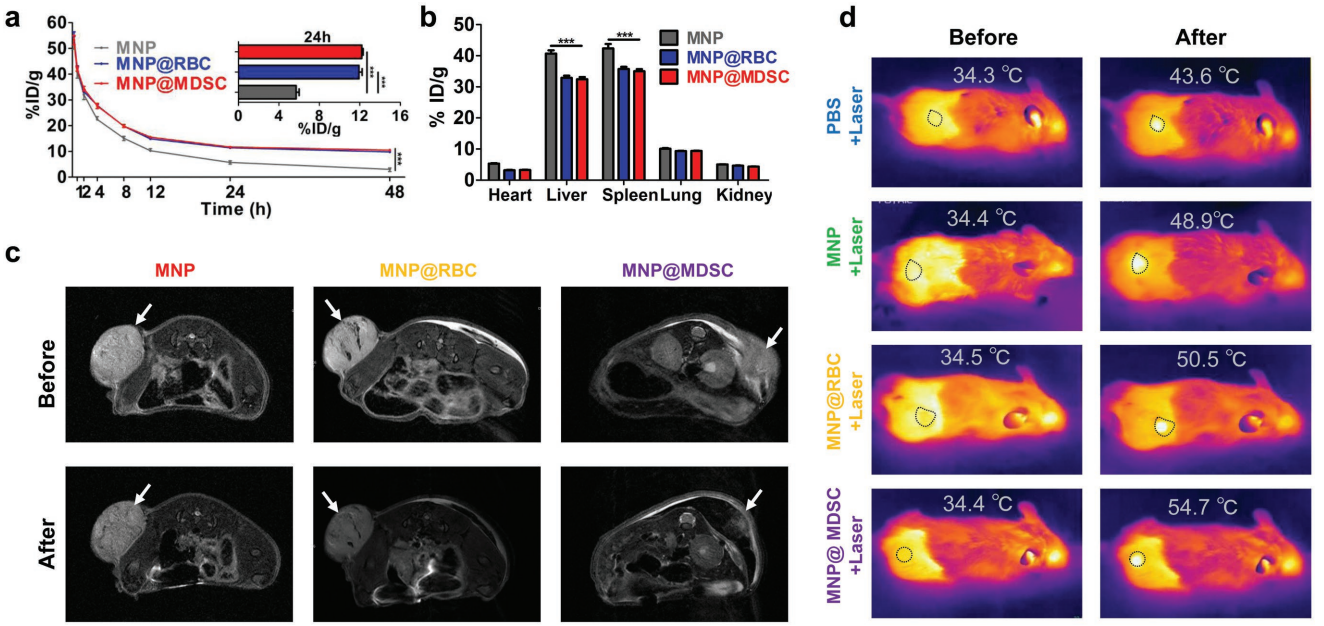


**Figure 3.** Targeting of MNPs to tumor sites for MR imaging and PTT. a) In vivo pharmacokinetic curves over a span of 48 h after intravenous injection of MNP, MNP@RBC, or MNP@MDSC into ICR mice. The inset is blood retentions of Fe content 24 h after injection. $n = 4$ in each group. b) Biodistribution of the nanoparticles 48 h after intravenous injection into ICR mice. $n = 4$ in each group. c) $T_2$-weighted MR images of B16/F10-tumor-bearing mice taken before and after injection of the nanoparticles. d) IR thermal images and tumor temperature measurements of B16-F10 tumor-bearing mice with or without intravenous injection of PBS, MNP, MNP@RBC, or MNP@MDSC, after exposure to an 808 nm laser at a power density of 5 W $cm^{-2}$ for 5 min. The circles indicate tumor sites. The data points represent mean ± s.d; ***, $p < 0.001$.

relaxation rate ($R_2$) of MNP@MDSC and MNP in magnetic resonance using a 7.0 T MRI instrument (Figure S5, Supporting Information). The result demonstrated that membrane coating did not impact $Fe_3O_4$ nanoparticles' MRI ability, suggesting the high potential of MNP@MDSC as a $T_2$-weighted MRI contrast agent. For in vivo MRI imaging, BALB/c nude mice bearing B16/F10 melanoma xenografts received 200 µL PBS containing MNP, MNP@RBC, or MNP@MDSC at a concentration of 5 mg $mL^{-1}$. At half an hour after injection, MRI was conducted on the same 7.0 T instrument. The mouse injected with MNP@MDSC yielded a fortified dark image at the tumor site in comparison to MNP@RBC and MNP group (Figure 3c), suggesting that MNP@MDSC has the most active and specific tumor-targeting out of the three nanoparticles. To demonstrate the use of MNP@MDSC for PTT, C57BL/6 mice bearing B16/F10 melanoma were injected with PBS or PBS containing MNP, MNP@RBC, or MNP@MDSC. Then the tumor site was irradiated with IR laser continuously for 5 min at half an hour after injection and temperatures at tumor surfaces were monitored using an IR camera. In the MNP@MDSC treatment group, the temperature of tumor surface increased from 34.4 to 54.7 °C (Figure 3d). This result is in good agreement with the superior tumor-targeting of MNP@MDSC compared with the other MNPs and demonstrates their potential value as an efficient PTT agent.

### 2.5. PTT-Inducing Immunogenic Cell Death (ICD) and Macrophages Polarization of MNP@MDSC

Indeed, analysis of protein expression in tumor tissues after PTT with laser irradiation showed enhanced tumor cell killing in the presence of MNP@MDSC, likely through PTT-induced ICD (a form of cell death). The immunogenic signature of ICD is the release of high-mobility group protein B1 (HMGB1), which can function as an "eat me" signal for the innate immune system, and exposure of Calreticulin and secretion of ATP.[15] In this study, we detected substantial levels of HMGB1 and Calreticulin after PTT in MNP@MDSC group compared with those of control group (**Figure 4**a; Figure S6, Supporting Information), indicating that MNP@MDSC combination with PTT significantly enhanced ICD. As MNPs were known to also induce macrophage state switch from M2 to M1, we set out to investigate whether the same could be achieved with MNP@MDSC. In vitro, coculture of cancer cells (B16/F10) and macrophages (RAW264.7) with or without nanoparticles (MNP or MNP@MDSC) shows that the sign of M1 macrophage associated gene expression (iNOS and CD86) was activated after nanoparticles treatment by reverse transcription polymerase chain reaction (RT-PCR). Conversely, the sign of M1 macrophage associated gene expression (Arginase 1 and CD206) was inhibited (Figure S9, Supporting Information). Further, we analyzed single-cell suspensions from lymph node, blood, and spleen with flow cytometry in vivo assay (Figure 4b). The results demonstrated that MNP@MDSC leads to M1 polarization of macrophage ($CD11b^+F4/80^+CD86^+$) and concomitant M2 ($CD11b^+F4/80^+CD206^+$) macrophages were decreased (Figure 4c,d; Figure S7, Supporting Information). Parallelly, immunofluorescence analysis of tumor sections showed that the numbers of $CD206^+$ M2 macrophages significantly reduced (Figure S8a, Supporting Information). Conversely, the numbers of $CD86^+$ M1 macrophages were significantly reduced in tumor microenvironment at MNP@MDSC group (Figure S8b,

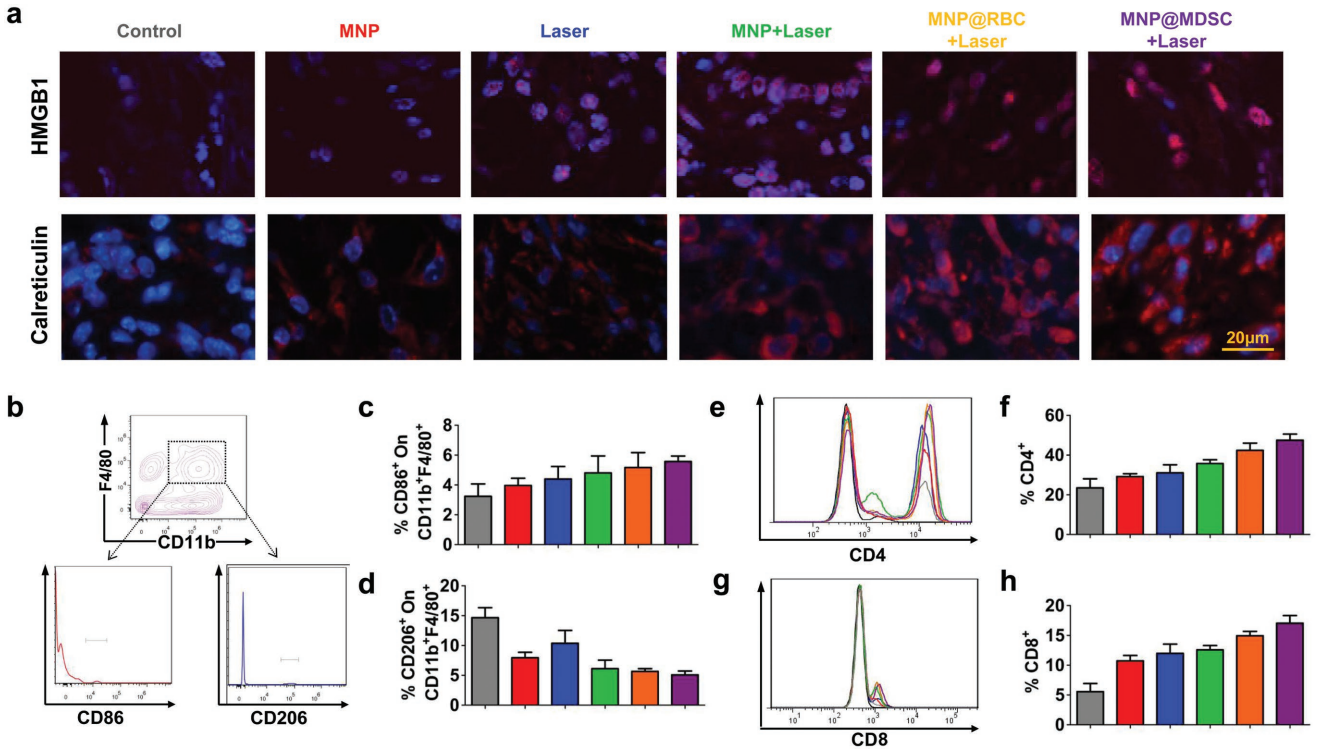


**Figure 4.** MNP-induced ICD and macrophage state switch. a) Representative images of mouse tumor slices stained for THMGB1 (top) and Calreticulin (bottom) after the indicated treatments. Scale bar = 20 μm. b) Representative flow cytometry plots of cell suspensions from the spleen using M1 ($CD86^+$) and M2 ($CD206^+$) macrophage markers. c) Percentage of $CD86^+$ cells within the $CD11b^+F4/80^+$ population of suspension cells from the mouse spleen after different treatments. d) Percentage of $CD206^+$ cells within the $CD11b^+F4/80^+$ population of suspension cells from the mouse spleen after different treatments. e) Representative flow cytometry images of CD4 positive cells from lymph node (LN). f) Quantification of CD4 positive cells in total cells in LN. g) Representative flow cytometry images of CD8 positive cells from LN. h) Quantification of CD8 positive cells on total cells in LN.

Supporting Information). Moreover, MNP@MDSC synergy with PTT significantly increased tumor infiltrating $CD8^+$ T cells compared with those of control groups (Figure S10, Supporting Information). Overall, these data indicated that antitumor immune response enhanced in MNP@MDSC treatment group.

### 2.6. In Vivo Antitumor Efficacy of MNP@MDSC

Based on these results, we then evaluated the antitumor effects of MNP@MDSC in C57BL/6 mice bearing B16/F10 melanoma. The mice were randomly divided into six groups and intravenously injected with different agents and intervention. The mice tumor volumes were measured every 3 d. The PBS group exhibited a rapid increase of tumor volume. Consistent with previous report, mice treated with MNP alone could inhibit tumor growth to some extent. However MNP themselves are insufficient to inhibit the tumor growth. The tumor-treated laser, MNP + laser, or MNP@RBC + laser also exhibit gradually strengthened tumor inhibition effects. Remarkably, tumor growth was nearly completely inhibited in MNP@MDSC + laser treatment group (**Figure 5**a). The coincident results are shown in the photographs of tumors (Figure 5b) and weight of tumor (Figure S11, Supporting Information). Besides, during treatment, the changes of body weight in MNP@MDSC treatment group were comparable to the rest of the group, indicating MNP@MDSC with a low risk of serious side effects (Figure 5c). With significant advances in mechanistic understanding of tumor biology, reprogramming of energy metabolic and evasion of immune destruction was added into the hallmarks of cancer.[16] In this study, we used an 18-fluoro-6-deoxy-D-glucose (FDG)-position emission tomography (PET) scanning analysis to evaluate the effects of MNP@MDSC on tumor metabolic activity.[17] The results showed that MNP@MDSC significantly inhibited tumor metabolic activity compared with those of control group (Figure 5d; Figure S12, Supporting Information), indicating that MNP@MDSC possesses high efficacy in antitumor. Furthermore, histological examination was used to evaluate the effect of antitumor. The results revealed that PTT significantly inhibited tumor proliferation and promoted tumor cells apoptosis in MNP@MDSC group, which are likely the results of decreased tumor metabolic rate and enhanced ICD (Figure 5e; Figure S13, Supporting Information).

## 3. Conclusions

In summary, we have designed and synthesized a novel MDSC membrane coated iron oxide nanoparticle and demonstrated its superior performance in immune escape, tumor-targeting, MR imaging, and PTT-induced tumor killing. Compared with MNP@RBC or naked MNP, MNP@MDSCs are much more effective in active tumor-targeting, a beneficial property afforded

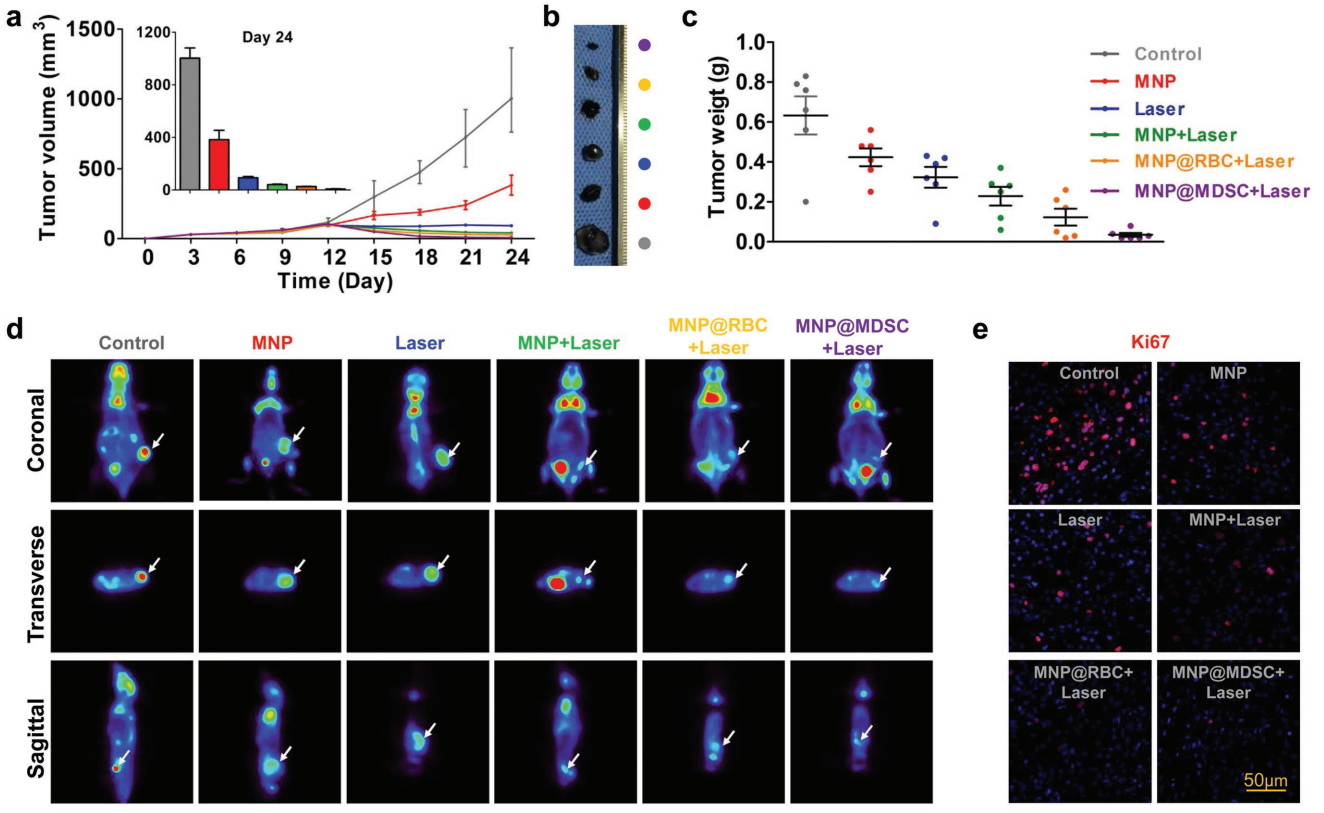


**Figure 5.** In vivo photothermal therapy. a) Growth (in volume) curves of mouse tumors in different treatment groups. b) Representative photographs of tumors from different treatment groups. c) Tumor weight in different treatment groups. d) F18-FDG PET images (coronal, transverse, and sagittal) of tumors in different treatment group. e) Representative images of mouse tumor slices stained for Ki-67 after different treatments. Scale bar = 50 μm.

by coating MNPs with membranes from naturally occurring MDSC, thus converting the MNPs into "smart" agents that like to accumulate in tumors as the original MDSCs. Once targeted to the tumor, MNP@MDSC can act as a PTT agent for enhanced antitumor response by inducing ICD, reprogramming the tumor-associated macrophages, and reducing the tumor metabolic activity. These benefits, in combination with the excellent biocompatibility and pharmacological kinetics characteristics, make MNP@MDSC a promising, multimodal agent for cancer theranostics.

## 4. Experimental Section

*Cells and Animal Models*: B16/F10 murine melanoma cells and RAW 264.7 murine macrophage-like cells were purchased from the American Type Culture Collection (ATCC, Manassas, VA) and genotype confirmed using STR sequence. Cell lines were maintained in Dulbecco's modified Eagle's medium (DMEM)/F12, 10% fetal bovine serum (FBS), at 5% $CO_2$, and 37 °C in a humidified incubator according to ATCC guidelines. ICR mice (male, 6–8 weeks old), BALB/c nude mice (female, 6–8 weeks old), and C57BL/6 mice (female, 6–8 weeks old) were purchased from Beijing Vital River Laboratory Animal Technology Co., Ltd. (China). BALB/c nude mice bearing B16-F10 melanoma xenografts were obtained by subcutaneous (s.c.) injection of 50 μL serum-free cell medium containing $5 \times 10^5$ B16/F10 cells into the shoulder of each mice. After the tumor formation, the tumor-bearing mice were used for MRI experiment. To establish melanoma-bearing C57BL/6 mouse model, B16/F10 cells ($1 \times 10^6$ cells in 200 μL serum-free cell medium) were inoculated subcutaneously into the flank of C57BL/6 mouse. After the tumor volume reached 50 $mm^3$, the tumor-bearing mice were used for further experiments. All the animal procedures were performed according to the guidelines of the Institutional Animal Care and Use Committee at Wuhan University.

*Myeloid-Derived Suppressor Cell Isolation*: Myeloid Derived Suppressor Sell Isolation Kit (mouse) was purchased from Miltenyi Biotec (Germany). First, single cell suspensions were obtained from the spleen of C57BL/6 mouse model. The MDSCs were indirectly magnetically labeled with Anti-Gr-1-Biotin and anti-Biotin microBeads. Then, the cell suspension was loaded on to a MACS Column, which is placed in the magnetic field of a MACS Separator. The magnetically labeled cells were retained with the column. After removing the column from the magnetic field, the magnetically labeled cells were collected in 15 mL centrifuge tube. To increase the purity of MDSCs, repeat the magnetic separation procedures as above described steps. Next, cells were fluorescently stained with CD11b-FITC (eBioscience, San Diego, CA) and Gr-1-PE (eBioscience, San Diego, CA) and analyzed by flow cytometry to confirm the purity of MDSCs. Cell debris and dead cells were excluded from the analysis based on scatter signals and propidium iodide fluorescence.

*Preparation of MDSC Membrane, MNP, and MNP@MDSC*: MDSC membrane, MNP, and MNP@MDSC were prepared as previously reported with slight modifications.[18]

*In Vivo Pharmacokinetics and Biodistribution*: To study the pharmacokinetics of particles, 16 ICR mice ($n$ = 4) received an intravenous (i.v.) injection of 200 μL PBS or PBS containing MNP, MNP@RBC, or MNP@MDSC at a dose of 25 mg Fe $kg^{-1}$. At various time points after the injection, 50 μL blood were collected via the tail veins, and then Fe content was quantified with ICP-AES. To study the biodistribution of the particles in various organs, all mice were euthanized on the fifth day after the injection and their hearts, livers,

spleens, kidneys, lungs, and blood were carefully collected. The blood was used for blood biochemical analysis. Partial organs were weighed and then Fe content of organs was quantified with ICP-AES.

*In Vivo Toxicity Evaluation*: In order to test the potential in vivo toxicity of MNP@MDSC, 20 ICR mice ($n = 5$) received an i.v. injection of 200 µL PBS, or PBS containing MNP, MNP@RBC, or MNP@MDSC at the concentration of 5 mg $mL^{-1}$. General status of the mice was evaluated every day by veterinarian and mice body weights were measured using a digital scale every 4 d. All mice were euthanized on the 24th d after the injection and their blood samples and major organs (i.e., hearts, livers, spleens, lungs, and kidneys) were collected. Three important hepatic indicators and two primary indicators for kidney functions were measured by using a blood biochemical autoanalyzer (7080, HITACHI, Japan). The complete blood panel data from healthy control and treated mice were also tested. Partial organs were fixed in 4% neutral buffered formalin, processed routinely into paraffin and sectioned at 4 µm. Then the sections were stained with H&E, and examined using an optical microscope (BX51, Olympus, Japan).

*In Vivo Chemotaxia Test*: In order to test MNP@MDSS active targeting tumor microenvironment, 12 BALB/c nude mice bearing B16-F10 tumor xenografts ($n = 4$) received an i.v. injection of 200 µL PBS containing MNP, MNP@RBC, or MNP@MDSC at a dose of 25 mg Fe $kg^{-1}$. At 24 h after the injection, all mice were anesthetized and then the tumors were excised from mice. Fe content in tumor was quantified with ICP-AES. Partial tumor specimens were stained with Prussian blue (Servicebio, Wuhan, China) and examined using an optical microscope (BX51, Olympus, Japan).

*In Vivo $T_2$-Weighted MRI*: In order to test in vivo MRI, nine BALB/c nude mice bearing B16-F10 tumor xenografts ($n = 3$) received an intravenous injection of 100 µL PBS containing MNP or MNP@MDSC at the concentration of 2.5 mg Fe $kg^{-1}$. Before and 0.5 h after the injection, all mice were evaluated by a 7.0 T Bruker PharmaScan animal instrument and $T_2$-weighted MR transversal cross-section images were collected utilizing a fast spin-echo sequence under the following parameters: TR = 2000 ms, TE = 36 ms, FA = 180°, matrices = 256 × 256, field of view (FOV) = 3.0 cm, slice thickness = 0.8 mm.

*In Vivo PTT Evaluation*: Sixteen tumor-bearing mice ($n = 4$) were i.v. injected with 100 µL PBS or PBS containing MNP, MNP@RBC, or MNP@MDSC at a dose of 2.5 mg Fe $kg^{-1}$. Half an hour after the injection, tumor sites of these mice were treated with the laser irradiation at 5 W $cm^{-2}$ for 5 min and then the temperatures of the tumor site were individually measured using an infrared (IR) thermographic camera (FORTRIC225, Shanghai Thermal Image Electromechanical Technology Co. Ltd., China).

*In Vivo Immunogenic Cell Death Evaluation*: Thirty C57BL/6 mice bearing B16-F10 tumor xenografts (≈150 $mm^3$ in volume) were randomly separated into six group ($n = 5$) and received an i.v. injection of 200 µL PBS (group 1), 200 µL PBS containing MNP (group 2), 200 µL PBS (group 3), 200 µL PBS containing MNP (group 4), 200 µL PBS containing MNP@RBC (group 5), and 200 µL PBS containing MNP@MDSC (group 6) at a dose of 25 mg Fe $kg^{-1}$ every 3 d. Half an hour after injection, the tumor sites (from group 3 to group 6) were treated with the laser irradiation at 5 W $cm^{-2}$ for 5 min. On the 24th d after the first injection, all mice were anesthetized by intraperitoneal (i.p.) injection of 80 µL 10% chloral hydrate solution and then the tumors were excised from mice. Partial tumor specimens were fixed in 4% neutral buffered formalin, processed routinely into paraffin and sectioned at 4 µm. Then, the tumor sections were stained with HMGB1 (Cell Signaling Technology) and Calreticulin (Abcam). The next day, slides were incubated with fluorochrome conjugated secondary antibodies (Alexa 594 anti-rabbit; Invitrogen) and nuclei were stained with DAPI (Vector Laboratories). Then, fluorescence images were captured through a CLSM-310, Zeiss fluorescence microscope.

*Flow Cytometry Analysis*: To analyze the polarization of macrophage in tumor microenvironment, the single cell suspension was incubated with anti-CD11b-FITC, anti-F4/80-Percp-Cy5.5, anti-CD206-APC, anti-CD86-PE (all from eBioscience, San Diego, CA) and isotype-matched IgG controls (eBioscience, San Diego, CA). Meanwhile, anti-CD4-FITC and anti-CD8-PE (eBioscience, San Diego, CA) antibodies were used for analysis of T cell. The results were disposed using FlowJo (Tree Star). 7AAD (Invitrogen) was used to exclude death cells.

*In Vivo Antitumor Effects Evaluation*: The mice body weight and tumor volumes (according to the formula (width$^2$ × length)/2) of 30 C57BL/6 tumor-bearing mice were individually measured after each treatment. On the 20th d after the first injection, all mice tumor metabolic were monitored using mouse micro-PET imaging system (Raycan Technology Company, Ltd., Suzhou, China). On the 24th d after the first injection, all mice were anesthetized and then the tumors were excised from mice. First, weight of tumor was measured. Then, partial tumor specimens were stained with Ki67 (Servicebio, Wuhan, China), TUNEL (Servicebio, Wuhan, China), and CD8 (Cell Signaling Technology). The next day, slides were incubated with fluorochrome conjugated secondary antibodies (Alexa 594 anti-rabbit, Alexa 488 anti-rabbit, Invitrogen) and nuclei were stained with DAPI (Vector Laboratories). Fluorescence images were then captured using a CLSM-310, Zeiss fluorescence microscope.

*Statistical Analyses*: Data analyses were performed using Graph Pad Prism version 5.0 for Windows (Graph Pad Software Inc., La Jolla, CA). Unpaired *t*-test and one-way ANOVA followed by the post-Tukey multiple comparison tests was used to analyze significant difference. Data were represented as the mean ± SEM. Differences ($P < 0.05$) were considered statistically significant.

Experimental details are provided in the Supporting Information.

## Supporting Information

Supporting Information is available from the Wiley Online Library or from the author.

## Acknowledgements

G.-T.Y. and L.R. contributed equally to this work. This work was supported by the National Natural Science Foundation of China (NFSC) (Grant Nos. 81672668, 81472528, 81472529), the Fundamental Research Funds for the Central Universities (2042017kf0171), and National Natural Science Foundation for Outstanding Youth Foundation (Grant No. 61722405). The authors appreciate Prof. Qing-Guo Xie, Huan-Huan Yan, and Chu-Ying Lei (Huazhong University of Science and Technology) for PET technological assistant. The authors also thank Fang Fang (National Center for Magnetic Resonance in Wuhan, State Key Laboratory of Magnetic Resonance and Atomic and Molecular Physics, Wuhan Institute of Physics and Mathematics, Chinese Academy of Sciences) for MRI technological assistant.

## Conflict of Interest

The authors declare no conflict of interest.

## Keywords

immunogenic cell death, macrophage, magnetic resonance imaging, myeloid-derived suppressor cell, photothermal therapy

Received: February 22, 2018
Revised: June 12, 2018
Published online: July 24, 2018

[1] a) R. L. Siegel, K. D. Miller, A. Jemal, *CA-Cancer J. Clin.* **2017**, *67*, 7; b) R. L. Siegel, K. D. Miller, A. Jemal, *CA-Cancer J. Clin.* **2016**, *66*, 7.
[2] a) K. Cho, X. Wang, S. Nie, Z. G. Chen, D. M. Shin, *Clin. Cancer Res.* **2008**, *14*, 1310; b) J. R. Heath, M. E. Davis, *Annu. Rev. Med.* **2008**, *59*, 251.

[3] a) Y. Cheng, L. Zhao, Y. Li, T. Xu, *Chem. Soc. Rev.* **2011**, *40*, 2673; b) M. Gao, C. Liang, X. Song, Q. Chen, Q. Jin, C. Wang, Z. Liu, *Adv. Mater.* **2017**, *29*; c) M. P. Sousa, S. G. Caridade, J. F. Mano, *Adv. Healthcare Mater.* **2017**, *6*; d) H. Chen, W. Zhang, G. Zhu, J. Xie, X. Chen, *Nat. Rev. Mater.* **2017**, *2*; e) J. Wang, W. Tao, X. Chen, O. C. Farokhzad, G. Liu, *Theranostics* **2017**, *7*, 3915; f) Z. Sun, Y. Zhao, Z. Li, H. Cui, Y. Zhou, W. Li, W. Tao, H. Zhang, H. Wang, P. K. Chu, X. F. Yu, *Small* **2017**, *13*; g) C. Wang, W. Sun, G. Wright, A. Z. Wang, Z. Gu, *Adv. Mater.* **2016**, *28*, 8912; h) S. T. Koshy, D. J. Mooney, *Curr. Opin. Biotechnol.* **2016**, *40*, 1.

[4] a) R. Chakravarty, H. F. Valdovinos, F. Chen, C. M. Lewis, P. A. Ellison, H. Luo, M. E. Meyerand, R. J. Nickles, W. Cai, *Adv. Mater.* **2014**, *26*, 5119; b) P. Martinkova, M. Brtnicky, J. Kynicky, M. Pohanka, *Adv. Healthcare Mater.* **2017**, *7*; c) H. Peng, J. Tang, R. Zheng, G. Guo, A. Dong, Y. Wang, W. Yang, *Adv. Healthcare Mater.* **2017**, *6*; d) M. Colombo, S. Carregal-Romero, M. F. Casula, L. Gutierrez, M. P. Morales, I. B. Bohm, J. T. Heverhagen, D. Prosperi, W. J. Parak, *Chem. Soc. Rev.* **2012**, *41*, 4306; e) L. Rao, B. Cai, L. L. Bu, Q. Q. Liao, S. S. Guo, X. Z. Zhao, W. F. Dong, W. Liu, *ACS Nano* **2017**, *11*, 3496; f) K. Yoo, B. G. Jeon, S. H. Chun, D. R. Patil, Y. J. Lim, S. H. Noh, J. Gil, J. Cheon, K. H. Kim, *Nano Lett.* **2016**, *16*, 7408.

[5] S. Zanganeh, G. Hutter, R. Spitler, O. Lenkov, M. Mahmoudi, A. Shaw, J. S. Pajarinen, H. Nejadnik, S. Goodman, M. Moseley, L. M. Coussens, H. E. Daldrup-Link, *Nat. Nanotechnol.* **2016**, *11*, 986.

[6] a) V. Bronte, S. Brandau, S. H. Chen, M. P. Colombo, A. B. Frey, T. F. Greten, S. Mandruzzato, P. J. Murray, A. Ochoa, S. Ostrand-Rosenberg, P. C. Rodriguez, A. Sica, V. Umansky, R. H. Vonderheide, D. I. Gabrilovich, *Nat. Commun.* **2016**, *7*, 12150; b) J. E. Talmadge, D. I. Gabrilovich, *Nat. Rev. Cancer* **2013**, *13*, 739.

[7] a) S. Solito, I. Marigo, L. Pinton, V. Damuzzo, S. Mandruzzato, V. Bronte, *Ann. N. Y. Acad. Sci.* **2014**, *1319*, 47; b) D. I. Gabrilovich, S. Ostrand-Rosenberg, V. Bronte, *Nat. Rev. Immunol.* **2012**, *12*, 253.

[8] a) D. Marvel, D. I. Gabrilovich, *J. Clin. Invest.* **2015**, *125*, 3356; b) D. Brusa, M. Simone, P. Gontero, R. Spadi, P. Racca, J. Micari, M. Degiuli, S. Carletto, A. Tizzani, L. Matera, *Int. J. Urol.* **2013**, *20*, 971; c) S. Ugel, F. De Sanctis, S. Mandruzzato, V. Bronte, *J. Clin. Invest.* **2015**, *125*, 3365.

[9] a) J. D. Lapek Jr., R. H. Fang, X. Wei, P. Li, B. Wang, L. Zhang, D. J. Gonzalez, *ACS Nano* **2017**, *11*, 11831; b) D. Huo, G. Liu, Y. Li, Y. Wang, G. Guan, M. Yang, K. Wei, J. Yang, L. Zeng, G. Li, W. Zeng, C. Zhu, *ACS Nano* **2017**, *11*, 10964; c) D. Dehaini, X. Wei, R. H. Fang, S. Masson, P. Angsantikul, B. T. Luk, Y. Zhang, M. Ying, Y. Jiang, A. V. Kroll, W. Gao, L. Zhang, *Adv. Mater.* **2017**, *29*; d) V. Balasubramanian, A. Correia, H. Zhang, F. Fontana, E. Makila, J. Salonen, J. Hirvonen, H. A. Santos, *Adv. Mater.* **2017**, *29*; e) J. Tang, D. Shen, T. G. Caranasos, Z. Wang, A. C. Vandergriff, T. A. Allen, M. T. Hensley, P. U. Dinh, J. Cores, T. S. Li, J. Zhang, Q. Kan, K. Cheng, *Nat. Commun.* **2017**, *8*, 13724; f) A. S. Cheung, D. J. Mooney, *Nano Today* **2015**, *10*, 511.

[10] a) L. Rao, L. L. Bu, B. Cai, J. H. Xu, A. Li, W. F. Zhang, Z. J. Sun, S. S. Guo, W. Liu, T. H. Wang, X. Z. Zhao, *Adv. Mater.* **2016**, *28*, 3460; b) L. Rao, L. L. Bu, L. Ma, W. Wang, H. Liu, D. Wan, J. F. Liu, A. Li, S. S. Guo, L. Zhang, W. F. Zhang, X. Z. Zhao, Z. J. Sun, W. Liu, *Angew. Chem., Int. Ed. Engl.* **2017**, *57*, 986; c) L. Rao, L. L. Bu, J. H. Xu, B. Cai, G. T. Yu, X. Yu, Z. He, Q. Huang, A. Li, S. S. Guo, W. F. Zhang, W. Liu, Z. J. Sun, H. Wang, T. H. Wang, X. Z. Zhao, *Small* **2015**, *11*, 6225; d) L. Rao, Z. He, Q. F. Meng, Z. Zhou, L. L. Bu, S. S. Guo, W. Liu, X. Z. Zhao, *J. Biomed. Mater. Res., Part A* **2017**, *105*, 521; e) L. Rao, Q. F. Meng, L. L. Bu, B. Cai, Q. Huang, Z. J. Sun, W. F. Zhang, A. Li, S. S. Guo, W. Liu, T. H. Wang, X. Z. Zhao, *ACS. Appl. Mater. Interfaces* **2017**, *9*, 2159.

[11] a) R. M. Hochmuth, C. A. Evans, H. C. Wiles, J. T. McCown, *Science* **1983**, *220*, 101; b) R. M. Hochmuth, N. Mohandas, P. L. Blackshear Jr., *Biophys. J.* **1973**, *13*, 747.

[12] S. Jin, S. Li, C. Wang, J. Liu, X. Yang, P. C. Wang, X. Zhang, X. J. Liang, *J. Biomed. Nanotechnol.* **2014**, *10*, 2393.

[13] D. Pardoll, *Annu. Rev. Immunol.* **2003**, *21*, 807.

[14] S. Barua, S. Mitragotri, *Nano Today* **2014**, *9*, 223.

[15] a) G. Gdynia, S. W. Sauer, J. Kopitz, D. Fuchs, K. Duglova, T. Ruppert, M. Miller, J. Pahl, A. Cerwenka, M. Enders, H. Mairbaurl, M. M. Kaminski, R. Penzel, C. Zhang, J. C. Fuller, R. C. Wade, A. Benner, J. Chang-Claude, H. Brenner, M. Hoffmeister, H. Zentgraf, P. Schirmacher, W. Roth, *Nat. Commun.* **2016**, *7*, 10764; b) M. Obeid, A. Tesniere, F. Ghiringhelli, G. M. Fimia, L. Apetoh, J. L. Perfettini, M. Castedo, G. Mignot, T. Panaretakis, N. Casares, D. Metivier, N. Larochette, P. van Endert, F. Ciccosanti, M. Piacentini, L. Zitvogel, G. Kroemer, *Nat. Med.* **2007**, *13*, 54; c) R. Kang, R. Chen, Q. Zhang, W. Hou, S. Wu, L. Cao, J. Huang, Y. Yu, X. G. Fan, Z. Yan, X. Sun, H. Wang, Q. Wang, A. Tsung, T. R. Billiar, H. J. Zeh III, M. T. Lotze, D. Tang, *Mol. Aspects Med.* **2014**, *40*, 1; d) W. J. Storkus, L. D. Falo Jr., *Nat. Med.* **2007**, *13*, 28; e) C. Clarke, M. J. Smyth, *Nat. Biotechnol.* **2007**, *25*, 192; f) E. Rapaport, J. Fontaine, *Proc. Natl. Acad. Sci. USA* **1989**, *86*, 1662; g) Y. Wang, I. Martins, Y. Ma, O. Kepp, L. Galluzzi, G. Kroemer, *Autophagy* **2013**, *9*, 1624.

[16] D. Hanahan, R. A. Weinberg, *Cell* **2011**, *144*, 646.

[17] a) K. Ott, W. A. Weber, F. Lordick, K. Becker, R. Busch, K. Herrmann, H. Wieder, U. Fink, M. Schwaiger, J. R. Siewert, *J. Clin. Oncol.* **2006**, *24*, 4692; b) H. A. Wieder, B. L. Brucher, F. Zimmermann, K. Becker, F. Lordick, A. Beer, M. Schwaiger, U. Fink, J. R. Siewert, H. J. Stein, W. A. Weber, *J. Clin. Oncol.* **2004**, *22*, 900.

[18] A. Parodi, N. Quattrocchi, A. L. van de Ven, C. Chiappini, M. Evangelopoulos, J. O. Martinez, B. S. Brown, S. Z. Khaled, I. K. Yazdi, M. V. Enzo, L. Isenhart, M. Ferrari, E. Tasciotti, *Nat. Biotechnol.* **2013**, *8*, 61.